DOI:
10.1002/mrm.27694

Document Version
Peer reviewed version

High-Dimensionality Undersampled Patch-Based Reconstruction (HD-PROST) for Accelerated Multi-Contrast Magnetic Resonance Imaging

Aurélien Bustin[1*], Gastao Cruz[1*], Olivier Jaubert[1], Karina Lopez[1], René M. Botnar[1,2], Claudia Prieto[1,2]

[1]Department of Biomedical Engineering, School of Imaging Sciences & Biomedical Engineering, King's College London, King's Health Partners, London, United Kingdom

[2]Escuela de Ingeniería, Pontificia Universidad Católica de Chile, Santiago, Chile

Short Title: HD-PROST reconstruction for accelerated multi-contrast MRI
Submitted as Full Paper to Magnetic Resonance in Medicine
Main document word count: 5036

[*]Aurélien Bustin and Gastao Cruz contributed equally to this study

Corresponding author:

Name	Aurélien Bustin, PhD
Department	Department of Biomedical Engineering
	School of Imaging Sciences & Biomedical Engineering
Institute	King's Health Partners, King's College London
Address	3rd Floor, Lambeth Wing, St Thomas' Hospital
	London SE1 7EH
	United Kingdom
E-mail	aurelien.bustin@kcl.ac.uk

ABSTRACT

Purpose: To develop a new high-dimensionality undersampled patch-based reconstruction (HD-PROST) for highly accelerated two-dimensional (2D) and three-dimensional (3D) multi-contrast magnetic resonance (MR) imaging.

Methods: HD-PROST jointly reconstructs multi-contrast MR images by exploiting the highly redundant information, on a local and non-local scale, and the strong correlation shared between the multiple contrast images. This is achieved by enforcing multi-dimensional low-rank in the undersampled images. 2D magnetic resonance fingerprinting (MRF) phantom and in vivo brain acquisitions were performed to evaluate the performance of HD-PROST for highly-accelerated simultaneous T_1 and T_2 mapping. Additional in vivo experiments for reconstructing multiple undersampled 3D Magnetization Transfer (MT)-weighted images were conducted to illustrate the impact of HD-PROST for high-resolution multi-contrast 3D imaging.

Results: In the 2D MRF phantom study, HD-PROST provided accurate and precise estimation of the T_1 and T_2 values in comparison to gold standard spin echo acquisitions. HD-PROST achieved good quality maps for the in vivo 2D MRF experiments in comparison to conventional low-rank inversion reconstruction. T_1 and T_2 values of white matter and grey matter were in good agreement with those reported in the literature for MRF acquisitions with reduced number of time-point images (500 time-point images, ~2.5sec scan time). For in vivo MT-weighted 3D acquisitions (6 different contrasts), HD-PROST achieved similar image quality than the fully-sampled reference image for an undersampling factor of 6.5-fold.

Conclusion: HD-PROST enables multi-contrast 2D and 3D MR images in a short acquisition time without compromising image quality. Ultimately, this technique may increase the potential of conventional parameter mapping.

Keywords: multi-contrast MRI; MR fingerprinting; patch-based reconstruction; low-rank tensor decomposition; compressed-sensing, magnetization transfer contrast

62

Introduction

In Magnetic Resonance Imaging (MRI), multiple contrasts are exploited to extract clinically relevant tissue parameters and pathological tissue changes. These multiple contrasts are achieved using different imaging sequences and preparation pulses. Multi-contrast acquisitions also find important applications in parameter mapping (e.g. T_1 and T_2 mapping) and magnetic resonance fingerprinting (MRF) (1,2). However these acquisitions lead to long scan times since multiple images with different contrasts need to be acquired, making parameter imaging more sensitive to physiological motion (3–6).

Parallel imaging (PI) (7–11), compressed sensing (CS) (12,13), as well as the combination of both undersampled reconstruction techniques (14,15) have been proposed to overcome the long scan times associated with multi-contrast imaging and parameter mapping. PI can accelerate multi-contrast imaging by undersampling each individual image and exploiting the information provided by multiple coil arrays, yet at a signal-to-noise ratio (SNR) penalty generally marked for high acceleration factors. Sparse CS alone has been shown to cope with the problem of undersampling through the use of random or pseudo-random sampling patterns and efficient regularized reconstructions which make the assumption that the multi-contrast images share common and sparse information in a specific domain (16–21). Even though these strategies have achieved acceleration factors that have not previously been possible to attain with parallel imaging alone, CS-based techniques still suffer from residual aliasing artifacts for high acceleration factors, which compromise the diagnostic value of the reconstructed multi-contrast images.

Recently, novel techniques that exploit the strong anatomical correlations observed in the contrast dimension (or parameter dimension) on a global or local scale have been proposed. Indeed, the nature of signal evolution in multi-contrast acquisitions exhibits a low-rank structure in the contrast dimension which can be exploited to further reduce scan times (17,22–24). These types of reconstruction techniques, also known as the globally (GLR) or locally low-rank (LLR) methods (25), have been efficiently used in many applications such as T_2 mapping (26) or dynamic contrast enhanced MRI (27). More recently, high-order

tensor decomposition techniques, exploiting global correlation, have been efficiently employed to allow for highly accelerated multi-dimensional cardiac MRI acquisitions (28,29). While those techniques have shown promise for motion-resolved quantitative cardiac imaging by efficiently solving a global low-rank tensor decomposition, they do not exploit the strong non-local correlations between neighboring patches.

Motivated by the LLR techniques which exploit localized correlations in the contrast dimension, patch-based image reconstructions exploiting non-local spatial redundancies and low-rank matrix structures have been introduced for single-contrast MRI reconstruction to lead to even sparser representation (30,31). By modeling the similarity of image patches through block-matching, low-rank representation and filtering, two-dimensional (2D) (32) and three-dimensional (3D) (33) patch-based reconstructions have been shown to outperform conventional CS reconstructions by recovering better image details and edges and exhibiting better overall image quality.

In this study, we present a new reconstruction technique for highly accelerated 2D and 3D multi-channel multi-contrast MRI which combines the promising performances of patch-based reconstructions and the potential of low-rank image reconstruction through higher-order tensor decomposition. The proposed High-Dimensionality undersampled Patch-based RecOnSTruction (HD-PROST) technique is first applied to accelerated 2D radial MRF, for various acceleration factors, where a high degree of inherent redundancy can be exploited locally, non-locally and through the contrast dimension. In a second application, HD-PROST is employed to acquire multiple undersampled high-resolution 3D Cartesian Magnetization Transfer Contrast (MTC) images with several MT weightings in a reduced scan time.

Theory

The framework presented hereafter jointly reconstructs multi-channel multi-contrast images from undersampled 2D or 3D MR acquisitions. This is achieved by generalizing

our previously proposed PROST technique (33) to high dimensional imaging. A description of the proposed HD-PROST reconstruction is presented, followed by the description of two multi-contrast applications (2D radial and 3D Cartesian) where high-dimensionality can be exploited to reduce acquisition time, which is often a key factor for clinical translation.

High-Dimensionality undersampled Patch-based RecOnStrucTion (HD-PROST)

Let $X \in \mathbb{C}^{M_x \times M_y \times M_z \times L}$ be the multi-contrast complex images that we seek to reconstruct, where M_x, M_y and M_z are the number of voxels in the x, y and z spatial directions, and L is the number of contrast-weighted images. The corresponding complex receive-coil sensitivity maps for the N_c channels are denoted as $S \in \mathbb{C}^{M_x \times M_y \times M_z \times N_c}$. Let $Y \in \mathbb{C}^{Z \times L \times N_c}$ be the undersampled k-space data (with $Z \ll M_x \times M_y \times M_z$). The joint multi-contrast undersampled reconstruction can be combined with parallel imaging and cast as the following inverse problem:

$$\underset{X}{\operatorname{argmin}} \frac{1}{2} \|AFSX - Y\|_F^2 \qquad [1]$$

where A is the undersampling operator that acquires k-space data for each contrast-weighted image, F denotes the Fourier transform operator and $\|\cdot\|_F$ is the Frobenius norm. Mathematically, this inverse problem is ill-posed, in the sense that the exact solution might not exist or not be unique, making precise recovery of X hardly possible, and prior assumptions on the unknown solution X have to be considered.

The principle behind HD-PROST reconstruction assumes that a multi-contrast image X can be expressed as a high-order low-rank representation on a patch scale, with respect to an appropriately chosen patch selection operator. The recovery problem can be formulated as the following constrained optimization on the high-order low-rank tensor $\mathcal{T}$:

$$\underset{X}{\operatorname{argmin}} \frac{1}{2} \|AFSX - Y\|_F^2 + \sum_p \lambda_p \left\|\mathcal{T}_p\right\|_* \quad s.t. \quad \mathcal{T}_p = P_p(X) \qquad [2]$$

where λ_p is the nonnegative sparsity-promoting regularization parameter and $\|\cdot\|_*$ is the nuclear norm that enforces multi-dimensional low-rank on a multi-contrast patch scale. The patch selection operator $P_p(\cdot)$ forms a 3D tensor from a patch centered at pixel p from a set of multi-contrast images (see optimization 2 below). Now considering the constraint $\mathcal{T}_p = P_p(X)$, and the encoding operator $E = AFS$, we can form the unconstrained Lagrangian of Equation 2 by linearly combining the constraint and cost function (31,33):

$$\begin{aligned} &\mathcal{L}_{HD-PROST}(X, \mathcal{T}, b) : \\ &= \underset{X,\mathcal{T},b}{\operatorname{argmin}} \frac{1}{2}\|EX - Y\|_F^2 + \sum_p \lambda_p \left\|\mathcal{T}_p\right\|_* \\ &+ \frac{\mu}{2}\sum_p \left\|\mathcal{T}_p - P_p(X) - \frac{b_p}{\mu}\right\|_F^2 \end{aligned} \quad [3]$$

where b is the Lagrange multiplier, and $\mu > 0$ is the penalty parameter. Equation 3 can be efficiently solved through operator-splitting via alternating direction method of multipliers (ADMM) (34). ADMM simplifies the optimization process by alternating the minimization with respect to the multi-contrast set of images X (optimization 1) and the high-order tensor $\mathcal{T}$ (optimization 2) followed by an update of the augmented multiplier b, and repeating these three steps until a convergence criterion is satisfied.

Optimization 1: Joint MR reconstruction update

The first sub-problem is a joint multi-contrast MR reconstruction that incorporates the denoised tensor $\mathcal{T}$ (obtained at the end of optimization 2) as prior information in a parallel imaging fashion to obtain X:

$$\mathcal{L}_{JointRecon}(X) := \underset{X}{\operatorname{argmin}} \frac{1}{2}\|EX - Y\|_F^2 + \frac{\mu}{2}\left\|\mathcal{T} - X - \frac{b}{\mu}\right\|_F^2 \quad [4]$$

Equation 4 corresponds to a standard iterative SENSE reconstruction with Tikhonov regularization, where the solution X can be efficiently computed using the Conjugate Gradient (35) algorithm.

158 *Optimization 2: High Order Singular Value Decomposition (HOSVD)-based denoising*

159 Considering the variable $\widetilde{\mathcal{T}_p} = P_p(X) + \frac{b_p}{\mu}$, the second sub-problem minimizes with respect
160 to the high-order tensor $\mathcal{T}$ and is given by

$$\mathcal{L}_{Tensor}(\mathcal{T}) := \underset{\mathcal{T}}{\operatorname{argmin}} \sum_p \frac{2\lambda_p}{\mu} \left\|\mathcal{T}_p\right\|_* + \sum_p \left\|\mathcal{T}_p - \widetilde{\mathcal{T}_p}\right\|_F^2 \qquad [5]$$

161 X denotes multiple MR images with different contrasts. Several observations can be made
162 about X: 1) on a local scale, voxels at a specific location for a given contrast exhibit similar
163 intensity to their nearest neighbors (within a patch); 2) on a non-local scale, images for a
164 given contrast contain self-repeating patterns (measured as patch similarity within a
165 neighborhood); and 3) on a contrast scale, common structures and features are shared across
166 multiple contrast images. Motivated by these observations, the proposed joint multi-
167 channel multi-contrast problem can be cast as a multi-dimensional low-rank reconstruction.
168 Bearing this in mind, equation 5 can be solved on a multi-contrast patch level. The
169 construction of the high-order tensor $\mathcal{T}$ is performed as a three-step process:

170 **Step 1 –** Similar overlapping patches in $X + \frac{b}{\mu}$ are grouped together to form a third-order
171 tensor: considering a $3D + L$ reference patch of size $N_x \times N_y \times N_z \times L$, we build a high
172 dimensional tensor $\widetilde{\mathcal{T}_p} \in \mathbb{C}^{N \times K \times L}$ of $K - 1$ similar $3D + L$ patches, with $N =$
173 $N_x \times N_y \times N_z$ (see Figure 1 – 'unfolding' and 'tensor stacking'). A fixed local window
174 is used for the patch search while the contrast signature remains unchanged. Along this
175 line, the proposed reconstruction can exploit as much of the contrast and spatial
176 correlations as possible.

177 **Step 2 –** The tensor $\widetilde{\mathcal{T}_p}$ exhibits a strong low multilinear rank structure and can therefore
178 be compressed into a tensor of smaller size (i.e. the core tensor) through tensor
179 decomposition (see Supporting Information Table S1 and Figure 1 – 'High-Order
180 Tensor Decomposition'). The dominant components of the core tensor can be extracted
181 by computing a complex-valued higher-order singular value decomposition (HOSVD)

(36,37) and by only keeping the largest (given by the thresholding parameter $\frac{2\lambda_p}{\mu}$) multilinear singular vectors and high-order singular values. This step effectively acts as a high-order denoising process where the small discarded coefficients mainly reflect contributions from noise and noise-like artifacts.

Step 3 – The denoised tensor $\mathcal{T}_p$ is then rearranged to form the denoised patches. Steps 1-3 are repeated over all patches in the image in a sliding window fashion. Since a single patch might belong to several groups in step 1, the final denoised multi-contrast complex-valued images $\mathcal{T}$ are obtained by averaging (Figure 1 – 'Aggregation') the different estimates.

The solution $\mathcal{T}$ to this optimization problem is a denoised version of $\tilde{\mathcal{T}}$ that is incorporated in the optimization 1 as prior knowledge, as described before. The Lagrangian multiplier b is then updated and optimizations 1 and 2 are processed iteratively to improve the quality of the reconstructed images. In the spirit of reproducible research, codes and examples for the proposed HD-PROST technique are made available at http://www.kclcardiacmr.com/downloads/.

The generalized reconstruction framework described before considers 2D or 3D Cartesian multi-contrast acquisitions (as the 3D undersampled Cartesian multi MT-weighted acquisitions considered in this study). Slight modifications in the reconstruction process are required for the accelerated non-Cartesian 2D MRF application considered in this study and will be described in the next section.

HD-PROST for Accelerated 2D Radial Parameter Mapping with MRF

MRF (1) is a novel quantitative MRI approach that allows the simultaneous acquisition of multi-parametric maps (e.g. T_1, T_2, M_0) in a single efficient scan. Conventional MRF sequences acquire in the order of thousand highly-undersampled time-point images by pseudo-randomly collecting the MR data in a continuous fashion with time-varying acquisition parameters (e.g. repetition time, flip angle). The spatial and temporal incoherencies provide a unique signal evolution (or fingerprint) for each tissue. These

unique fingerprints can be matched, through pattern matching, to a pre-generated MRF dictionary representative of the MRF sequence, and whose atoms are composed of simulated signal evolution curves. This matching process is performed on a voxel-by-voxel basis to identify the underlying tissue properties and generate quantitative parameter maps. The highly-undersampled pseudo-random MRF acquisition results in a high level of noise and aliasing in the reconstructed time-point images. Several iterative techniques have been recently proposed to improve the reconstruction quality of each time-point image (38–42). Zhao et al. proposed to enforce low-rank and subspace modeling in the temporal dimension to reconstruct high-quality time-point images (38). Assländer et al. recently introduced a low-rank ADMM reconstruction technique to temporally compress the time-point images, resulting in a reduced number of singular value images. The reconstruction of the temporally compressed images is faster and better posed than reconstructing each time-point image separately (39). This temporal compression operator U_r is obtained through compression of the MRF dictionary at an appropriate rank r. Due to the multi-contrast nature of MRF, HD-PROST can be used to explicitly exploit the local, non-local and contrast information of the temporally compressed images by integrating the compression operator into the encoding operator in Equation 3 as follows:

$$E_{MRF} = AU_rFS \qquad [6]$$

Methods

The proposed HD-PROST reconstruction was evaluated on accelerated radial 2D MRF phantom and in vivo brain acquisitions, and on accelerated Cartesian 3D magnetization transfer imaging with varying MT-weighting in in vivo brain data. The two applications are described in detail below along with imaging and reconstruction parameters. Written informed consent was obtained from all subjects before undergoing MRI scans and the study was approved by the Institutional Review Board.

Accelerated 2D Magnetic Resonance Fingerprinting

MRF acquisitions were performed on a 1.5T Ingenia MR system (Philips, Best, The Netherlands) equipped with a 15-element head coil.

Phantom and In Vivo Experiments

A 2D MRF acquisition was performed on a standardized (T1MES) T_1/T_2 phantom containing nine agarose-based tubes with different T_1 and T_2 combinations (range, T_1: 255 ms to 1489 ms, T_2: 44 ms to 243 ms) (43). Relevant scan parameters included: balanced steady-state free precession radial sequence, echo time (TE) = 2 ms, fixed repetition time (TR) = 4.4 ms, field-of-view (FOV) = 160x160 mm^2, in-plane resolution = 1x1 mm^2, slice thickness = 8 mm, bandwidth = 723.4 Hz/pixel. Only one radial spoke was acquired at each time-point (resulting in an acceleration factor of about 251 with respect to a fully-sampled radial acquisition). A total of 2000 time-points were acquired in 10 seconds. A flip angle (FA) pattern similar to the one proposed in (44) for optimized T_1/T_2 mapping was used, and is shown in Supporting Information Figure S1. This RF pattern, which has been shown to be optimal in a Cramér-Rao lower bound sense, consists of intrinsic repetitive loops which offers the advantage to lengthen the scan time by simple concatenation. The experiments consisted of undersampling the acquired data by keeping only $[1:n]$ k-space radial spokes, with $n = [400:100:2000]$, resulting in scan time reductions up to a factor of 5 with respect to the 2000 time-points sequence.

Reference T_1 and T_2 times for each vial were obtained from gold standard spin echo (SE) acquisitions. For T_1 values, an inversion-recovery SE (IRSE) sequence was used with eight inversion times from 25 ms to 3200 ms with TR = 10s, TE = 14.75ms. For T_2 values, the SE sequence was performed with eight TEs from 10 ms to 640 ms. T_1 and T_2 values were obtained by mono-exponential curve fitting.

Single slice 2D MRF brain data were acquired in five healthy subjects (four men, mean age: 32 years; range: 28-37 years) using the same scan parameters as in the phantom experiments.

Image Reconstruction

For both phantom and in vivo 2D MRF experiments, data was temporally compressed with $r = 10$, leading to only 10 singular value images to reconstruct (i.e. in this study, $L = 10$ and $M_z = 1$).

HD-PROST reconstruction was implemented using the algorithm described in Supporting Information Table S2 and performed offline on a workstation with a 16-core Dual Intel Xeon Processor (23 GHz, 256 GB RAM). The joint MR reconstruction step (optimization 1) was implemented in Matlab (v7.1, MathWorks, Natick, MA) and the multi-contrast patch-based denoising step (optimization 2) in C++. Coil sensitivity maps were estimated using the eigenvalue-based approach ESPIRiT (45).

The encoding operator E_{MRF} was implemented using the nonuniform fast Fourier transform (46). The tolerance of the conjugate gradient was set to $CG_{eps} = 1e^{-4}$ and a maximum number of $CG_{iter} = 15$ iterations was chosen as stopping criterion. The regularization parameter μ, which balances the contribution of the prior term (obtained at the end of optimization 2) and the data fidelity term, was set to $5e^{-3}$.

The proposed high-order patch-based denoising strategy was implemented as described in Supporting Information Table S1. The performance of the proposed strategy relies on the optimal selection of several parameters. The patch size, which controls the degree of local image features, was set to $N = 7 \times 7$. We set the search window radius around each pixel to 20 and restricted the number of similar patches selected to $K = 20$ to form a third-order tensor $\mathcal{T}_p$ of size $49 \times 20 \times 10$. The l_2 distance was chosen as measure of patch similarity and was defined as $d(patch_{ref}, patch_j) = \|patch_{ref} - patch_j\|_2$ for $j = 1, \dots, K-1$. In order to save computational complexity, a sliding-window approach was performed with a patch offset of 3 pixels at each image dimension. The performance of HD-PROST was assessed on several data sets (not reported here) by comparing the quality of the reconstructions with several regularization parameters λ (the same λ was used for all patches: $\lambda_p = \lambda$ for all p). The optimal value was shown to be proportional to the number of MRF measurements and was set to $\lambda = -1e^{-3} \times n + 0.4$ for each decomposition, with

n being the number of MRF radial spokes. The joint MR reconstruction and denoising steps were iteratively interleaved and the reconstruction was terminated after five ADMM iterations. All parameters were empirically optimized on one dataset by visual inspection and the same values were used for all other subjects.

The proposed HD-PROST reconstruction for 2D MRF was compared to the low-rank inversion (LRI) reconstruction (24,38) with $r = 10$ and using 10 conjugate gradient iterations, which were seen to be enough for convergence.

Dictionary generation and pattern recognition

The MRF dictionary was generated using the Extended Phase Graphs (EPG) formalism (47). The dictionary was calculated for a T_1 in the range of ($[50{:}\,10{:}\,1400, 1430{:}\,30{:}\,1600, 1700{:}\,100{:}\,2200, 2400{:}\,200{:}\,3000]$ ms) and T_2 in the range of ($[5{:}\,2{:}\,80, 85{:}\,5{:}\,150, 160{:}\,10{:}\,300, 330{:}\,30{:}\,600]$ ms). Slice profile was simulated for each RF pulse using 51 isochromats distributed along the slice selection direction and was included in the dictionary generation to correct for profile imperfections (48). Template matching between fingerprints and dictionary were performed using the inner product as in (1).

Accelerated 3D Multi-Contrast Magnetization Transfer Imaging

Acquisition

A 3D accelerated MTC experiment was performed to evaluate the proposed HD-PROST reconstruction on 3D Cartesian acquisitions with multiple MT-weighted images. In vivo brain acquisitions were performed on three healthy subjects (one man, age range: 24-30 years) on a 1.5T MR scanner (Magnetom Aera, Siemens Healthcare, Erlangen, Germany) equipped with a 20-channel head coil. Acquisitions consisted of one reference image without magnetization preparation, and five images with different MT preparations (i.e. in this study, $L = 6$ and $M_z > 1$).

A prototype 3D Cartesian variable-density trajectory was integrated in the sequence to allow for fast acquisition of multiple MT-weighted images. The Cartesian trajectory with spiral profile order (33,49) samples the k_y-k_z phase-encoding plane following approximate spiral interleaves on the Cartesian grid with variable density along each spiral arm and with two successive spiral interleaves being rotated by the golden ratio. A golden angle rotation between different contrast acquisitions was incorporated here (shifted VD-CASPR) to introduce incoherently distributed aliasing artifacts along the contrast dimension and noise-like artifacts in the spatial dimension, which is beneficial from a CS and low-rank point of view (50).

The MT weighting was achieved by applying a train of sinc-shaped, off-resonance RF pulses before image acquisition with the following parameters: MT off-resonance frequency (ΔF) = 3 kHz, 20 MT pulse repetitions, MT bandwidth = 401 Hz/pixel. Relevant scan parameters included: 3D gradient echo sequence, axial orientation, FOV = 230x230x160 mm^3, nominal resolution 1x1x2 mm^3, FA = 15°, TE = 1.78 ms, TR = 4.06 ms, receiver bandwidth = 925 Hz/pixel, 32 readouts per spiral interleave. Six measurements were acquired with different MT pulse flip angles ($\alpha_{MT} = [0°, 160°, 320°, 480°, 640°, 800°]$) with five seconds pause between them. Acquisitions were performed with an acceleration factor of 6.5-fold for each weighted image. The total scan time to acquire the six measurements was 13:18 [min:sec]. A fully-sampled acquisition of the six measurements at this resolution would take more than one hour. Therefore, for comparison purposes, an additional fully-sampled acquisition was performed only for the reference image ($\alpha_{MT} = 0°$). The total scan time for this single-contrast fully-sampled acquisition was 12:57 [min:sec].

Reconstruction

The following parameters were used for the 3D multi-MT reconstruction: patch size $N = 7 \times 7 \times 7$, search window = $20 \times 20 \times 20$, number of similar 3D patches selected $K = 30$, patch offset = 3, ADMM iterations = 5, $CG_{eps} = 1e^{-7}$, $CG_{iter} = 10$. The threshold parameters λ and μ were empirically set to 0.1 and $5e^{-3}$, respectively. Coil sensitivity maps

were estimated from the fully-sampled k-space center using the eigenvalue-based approach ESPIRiT.

The proposed HD-PROST reconstruction was compared with two well-established state-of-the-art reconstruction techniques. The first technique is LLR, proposed by T. Zhang (26) for accelerating MR parameter mapping. LLR exploits the redundancy in the contrast dimension on local image regions in an iterative low-rank framework. LLR was implemented using our ADMM framework by replacing the patch-based denoising step by the low-rank thresholding. This allows for fair comparisons since the same optimization was used and only the manner in which the denoising is performed was modified. The rank threshold λ_{LLR} was fixed and set to 5% of the highest singular value. Since the acquired MT-weighted data was fully-sampled in the read-out direction, the MR reconstruction step was accelerated for both LLR and HD-PROST reconstructions by computing a one-dimensional inverse FFT and considering multiple separable 2D reconstruction problems independently.

The second technique is an iterative CS reconstruction with spatial Wavelet sparsity constraint as described in (12) and implemented in the BART toolbox (51). CS reconstruction was performed for each contrast independently. The regularization parameter λ_{CS} was optimized experimentally and set to 0.01. Visual assessment was performed between the different techniques and the fully-sampled acquisition.

Results

Accelerated 2D Magnetic Resonance Fingerprinting

Phantom study

Figure 2 shows T_1 and T_2 values for the 2D MRF phantom experiments with 2000, 1000 and 500 time-points in comparison to the gold standard IRSE and SE acquisitions for both LRI and HD-PROST reconstructions. T_1 values obtained from both strategies were in good

agreement with the IRSE acquisition even for reconstructions with 500 time-points, with an excellent linear relationship with the reference T_1 values (goodness-to-fit $R^2 > 0.98$). T_2 accuracy was also preserved with the proposed reconstruction with a slight T_2 degradation observed for long T_2 values and high acceleration for both reconstructions. Figure 3 depicts the precision of T_1 and T_2 values, as characterized by the standard deviation (aggregated based on the variance of each vial). An increase in precision was observed for both T_1/T_2 values using the proposed HD-PROST reconstruction compared with LRI even for reconstructions with 500 time-points, corresponding to 2.5s scan time. Corresponding T_1 and T_2 maps are shown in Supporting Information Figure S2. From the above analysis, it follows that 500 MRF time-points or less might be sufficient and suitable for accurate and precise in vivo T_1/T_2 maps acquisitions in less than 2.5 seconds.

In vivo study

Figure 4 depicts the first four 2D MRF singular images from the reference LRI and the proposed HD-PROST reconstruction for one representative subject reconstructed with 1000 time-points. A clear superior image quality can be observed on the HD-PROST singular images with a sharp and clear delineation of the brain structures. A high level of streaking artifacts and noise can be seen on the last singular value components (e.g. singular images #3 and #4) with LRI, whereas HD-PROST not only produces images with considerably less noise but is also able to recover small structures that were lost below the noise level with LRI (Figure 4, yellow arrows). T_1 and T_2 maps are displayed in Figure 5 and Figure 6 for two subjects and three different measurement lengths (2000, 1000 and 500 time-points) for both LRI and HD-PROST reconstructions.

The reconstructed maps from one additional subject are shown in Supporting Information Figure S3. A number of interesting observations can be made. Reducing the number of measurements tends to blur the T_1 maps with LRI while the T_2 maps suffer from noise amplification, showing an overall noisier appearance. Conversely, by enforcing low-rank in the local, non-local and contrast dimension, HD-PROST reconstruction delivers higher image quality, recovering sharpness for T_1 and reducing the noise for T_2. The improvement

is more pronounced for the 500 time-points acquisition (2.5s scan time). In vivo T_1 and T_2 relaxation times measured in regions of interest in the white and grey matters with LRI and the proposed HD-PROST are shown in Table 1. Both reconstructions converged to very comparable values that are in good agreement with values obtained from the literature for T_1. Moreover, the proposed HD-PROST reconstruction tends to lower the standard deviations of T_1 and T_2 times, which is in accordance with the noise reduction seen in the quantitative maps. Note that the T_2 relaxation times for both techniques are slightly biased and depart from the literature values. This may be partly explained by the fact that B_1 imperfections (52) as well as other sources of bias such as magnetization transfer (53) and diffusion-weighting (54) were not considered in the proposed study. The average reconstruction time for 2D MRF with HD-PROST was about 10 minutes per data set. Additional comparisons with single-contrast PROST reconstruction (i.e. reconstructing each singular image independently) and with a global low-rank tensor decomposition (in the spirit of cardiac multitasking (28,29)) are provided in Supporting Information Figure S4.

Accelerated 3D Multi-Contrast Magnetization Transfer Imaging

Figure 7 depicts four axial slices obtained with HD-PROST reconstruction of the 6.5-fold undersampled 3D MT-weighted images in a representative subject in comparison to the fully-sampled acquisition. Only the reference image obtained with $\alpha_{MT} = 0°$, is shown here. Similar image quality is observed between the 6.5-fold accelerated HD-PROST approach and the fully-sampled scan. Line profiles going through a structure with sharp edges are shown in Figure 7c, showing excellent agreement between HD-PROST and the fully-sampled reference. Six different undersampled MT-weighted images were acquired in 13min 18s, whereas the fully-sampled acquisition of a single contrast took 12min 57s. Figure 8 compares HD-PROST to conventional CS reconstruction from a 6.5-fold acceleration. Comparisons with zero-filling and LLR reconstructions are provided in Supporting Information Figures S5 and S6. As expected, zero-filling exhibits a low image

quality with apparent aliasing artifacts and blurring. Exploiting contrast redundancy through local image regions with LLR improves the overall image quality and enables the recovery of small structures, particularly for low-contrast images (e.g. $\alpha_{MT} = 800°$), while the apparent noise is still large. By contrast, CS reconstruction with spatial regularization is able to recover images with reduced level of noise but fails to recover small structures for low contrast images (see Figure 8, red arrows). Enforcing multi-dimensional low-rank and capturing 3D information of local and non-local 3D patches through the multiple MT-weighted images with HD-PROST allows to recover small structures and reduced the level of apparent noise, resulting in high image quality for all different contrasts. Reconstructions from two other subjects can be seen in Supporting Information Figures S7 and S8. The average computation time for 3D HD-PROST reconstruction was about 27 minutes for all 6 contrasts in the acquisitions performed in this study.

Discussion

HD-PROST reconstruction enables accelerated acquisition of 2D or 3D multi-contrast MR images by exploiting the high local and non-local redundancies, and the similarities between the multi-contrast images through a high-order low-rank tensor approximation.

The proposed technique was applied to accelerated non-Cartesian 2D MRF and accelerated Cartesian 3D MTC imaging to enable undersampling factors that go beyond the limit of traditional PI and CS reconstructions (i.e. about 2.5 seconds acquisition for 2D MRF, and 6.5-fold acceleration for 3D MTC), while removing residual aliasing artifacts. Phantom experiments in accelerated 2D MRF were carried out to investigate the impact of rapid acquisition (i.e. reduced number of time-point images) on accuracy and precision of T_1 and T_2 relaxation times. High agreement with reference T_1/T_2 values was observed using HD-PROST, even for high accelerations, with increased precision compared to conventional LRI reconstruction.

For in vivo MRF, streaking artifacts and noise amplification often propagated in the T_1 maps with LRI reconstruction, while blurring was observed on the T_2 maps for high acceleration factors. HD-PROST achieved improved sharpness and reduced noise level in comparison to the low-rank inversion reconstruction, especially for acquisitions with reduced number of time-points. Nevertheless, a systemic underestimation of the T_2 values, previously reported in MRF literature, was observed in the in vivo study. This finding may be partly explained by the fact that B_1 imperfections (52), magnetization transfer (53), and diffusion-weighting (54) were not considered in this MRF study and could lead to inaccurate T_2 measurements.

HD-PROST has a modular design, which allows for its straightforward extension to 3D or n-D imaging by simple patch vectorization. In line with the previous 2D MRF study, accelerated 3D MTC using HD-PROST showed improved image quality over conventional CS and low-rank reconstructions for an acceleration factor of 6.5, with visual quality comparable to the fully-sampled acquisition. High denoising performance was achieved due to the existence of multiple MT-weighted images of the same object with varying contrasts, leading to high redundancy which can be exploited by HD-PROST. The pseudo-random sampling, given by the proposed shifted VD-CASPR, causes aliasing artifacts that spread incoherently in the contrast dimension and exhibits noise-like perturbations at the image scale, providing an excellent basis for HD-PROST reconstruction. This study was only performed on a small number of subjects and further evaluations on larger cohorts are needed. Nevertheless, this proof of concept suggests an opportunity for high-resolution quantitative magnetization transfer imaging in a clinically feasible scan time.

The efficient multithreaded implementation of the high-order patch-based denoising allowed for fast image denoising of large data sets (e.g. in the order of 200 seconds for a 3D data set with a matrix size of $200 \times 256 \times 104 \times 6$). Further speedups could be achieved to reach clinically acceptable runtimes by implementing the joint MR optimization step on multiple GPUs (55) and using coil compression algorithms (56).

HD-PROST imposes low-rank in the complex domain, and therefore captures the possible cross-correlation observed between the real and imaginary components, allowing for accurate and faithful reconstruction of both phase and magnitude. Our framework makes use of ADMM to decouple the main optimization problem into two simpler sub-problems that have straightforward solutions. Although most of the noise and undersampling artifacts can be efficiently removed after the first iteration, aliasing may still exist depending on the quality of the input images. This behavior mainly stems from the fact that corrupted images can negatively affect the block matching step, resulting in a sub-optimal grouping. Thus, several ADMM iterations (five in this study) are needed to achieve good image quality reconstructions.

The technique proposed in this paper can potentially change conventional multi-contrast imaging by making efficient use of the rich and redundant information available locally and temporally. Two applications were introduced in this study, nonetheless HD-PROST stays generic and should be easily extendable to many MR applications where multiple contrasts are involved, such as conventional T_1 and T_2 mapping, perfusion imaging (57), 4D flow MRI (58) or low SNR applications such as arterial spin labeling (59).

Conclusion

We present a new framework, termed HD-PROST, for efficient reconstruction of undersampled multi-channel multi-contrast MR images. HD-PROST aims at achieving high image quality by exploiting the high local and non-local redundancies, and the similarities between the multi-contrast images through a high-dimensionality low-rank tensor decomposition. HD-PROST was validated in accelerated 2D MRF to generate precise T_1 and T_2 maps in about 2.5 seconds without affecting T_1/T_2 accuracy. For accelerated multiple 3D MT-weighted acquisitions, HD-PROST can recover high quality images, comparable to a fully-sampled acquisition, in a clinically reasonable timeframe. The straightforward, yet efficient, application of HD-PROST to 2D and 3D multi-contrast data sets, provides several opportunities for future research, particularly in areas where high-dimensionality is likely to increase in importance.

Acknowledgement

The authors would like to thank Dr. Radhouene Neji (Siemens Healthcare, Frimley, United Kingdom) and Dr. Torben Schneider (Philips Healthcare, United Kingdom) for their assistance in the implementation of the MR sequences presented in this study. The authors acknowledge financial support from: (1) EPSRC EP/P001009/, EP/P032311/1, EPSRC EP/P007619, (2) Wellcome EPSRC Centre for Medical Engineering (NS/ A000049/1), and (3) the Department of Health via the National Institute for Health Research (NIHR) comprehensive Biomedical Research Centre award to Guy's & St Thomas' NHS Foundation Trust in partnership with King's College London and King's College Hospital NHS Foundation Trust. The views expressed are those of the authors and not necessarily those of the NHS, the NIHR or the Department of Health.

References

1. Ma D, Gulani V, Seiberlich N, Liu K, Sunshine JL, Duerk JL, Griswold MA. Magnetic resonance fingerprinting. Nature [Internet] 2013;495:187–92. doi: 10.1038/nature11971.

2. Jiang Y, Ma D, Seiberlich N, Gulani V, Griswold MA. MR fingerprinting using fast imaging with steady state precession (FISP) with spiral readout. Magn. Reson. Med. 2015;74:1621–1631. doi: 10.1002/mrm.25559.

3. Xue H, Shah S, Greiser A, Guetter C, Littmann A, Jolly M-P, Arai AE, Zuehlsdorff S, Guehring J, Kellman P. Motion correction for myocardial T1 mapping using image registration with synthetic image estimation. Magn. Reson. Med. [Internet] 2012;67:1644–1655. doi: 10.1002/mrm.23153.

4. Roujol S, Basha TA, Weingärtner S, Akçakaya M, Berg S, Manning WJ, Nezafat R. Impact of motion correction on reproducibility and spatial variability of quantitative myocardial T2mapping. J. Cardiovasc. Magn. Reson. 2015;17. doi: 10.1186/s12968-015-0141-1.

5. Cruz G, Jaubert O, Schneider T, Botnar RM, Prieto C. Rigid Motion Corrected Magnetic Resonance Fingerprinting. Magn. Reson. Med. 2019;81:947–961. doi: https://doi.org/10.1002/mrm.27448.

6. Mehta BB, Ma D, Pierre EY, Jiang Y, Coppo S, Griswold MA. Image reconstruction algorithm for motion insensitive MR Fingerprinting (MRF): MORF. Magn. Reson. Med. 2018:1–16. doi: 10.1002/mrm.27227.

7. Pruessmann KP, Weiger M, Scheidegger MB, Boesiger P. SENSE: sensitivity encoding for fast MRI. Magn. Reson. Med. [Internet] 1999;42:952–62. doi: 10.1002/(SICI)1522-2594(199911)42:5<952::AID-MRM16>3.0.CO;2-S.

8. Griswold M a, Jakob PM, Heidemann RM, Nittka M, Jellus V, Wang J, Kiefer B, Haase A. Generalized autocalibrating partially parallel acquisitions (GRAPPA). Magn. Reson. Med. [Internet] 2002;47:1202–10. doi: 10.1002/mrm.10171.

544 9. Lustig M, Pauly JM. SPIRiT: Iterative self-consistent parallel imaging
545 reconstruction from arbitrary k-space. Magn. Reson. Med. [Internet] 2010;64:457–
546 71. doi: 10.1002/mrm.22428.
547 10. Bilgic B, Kim TH, Liao C, Manhard MK, Wald LL, Haldar JP, Setsompop K.
548 Improving parallel imaging by jointly reconstructing multi-contrast data. Magn.
549 Reson. Med. 2018;80:619–632. doi: 10.1002/mrm.27076.
550 11. Li Y, Dumoulin C. Correlation imaging for multiscan MRI with parallel data
551 acquisition. Magn. Reson. Med. 2012;68:2005–2017. doi: 10.1002/mrm.24206.
552 12. Lustig M, Donoho D, Pauly JM. Sparse MRI: The application of compressed
553 sensing for rapid MR imaging. Magn. Reson. Med. [Internet] 2007;58:1182–95. doi:
554 10.1002/mrm.21391.
555 13. Doneva M, Börnert P, Eggers H, Stehning C, Sénégas J, Mertins A. Compressed
556 sensing reconstruction for magnetic resonance parameter mapping. Magn. Reson.
557 Med. [Internet] 2010;64:1114–20. doi: 10.1002/mrm.22483.
558 14. Velikina J V., Alexander AL, Samsonov A. Accelerating MR parameter mapping
559 using sparsity-promoting regularization in parametric dimension. Magn. Reson.
560 Med. 2013;70:1263–1273. doi: 10.1002/mrm.24577.
561 15. Gong E, Huang F, Ying K, Wu W, Wang S, Yuan C. PROMISE: Parallel-
562 imaging and compressed-sensing reconstruction of multicontrast imaging using
563 SharablE information. Magn. Reson. Med. [Internet] 2014;73:523–535. doi:
564 10.1002/mrm.25142.
565 16. Bilgic B, Goyal VK, Adalsteinsson E. Multi-contrast reconstruction with
566 Bayesian compressed sensing. Magn. Reson. Med. [Internet] 2011;66:1601–15. doi:
567 10.1002/mrm.22956.
568 17. Zhang L, Athavale P, Pop M, Wright GA. Multicontrast reconstruction using
569 compressed sensing with low rank and spatially varying edge-preserving constraints
570 for high-resolution MR characterization of myocardial infarction. Magn. Reson.

Med. 2017;78:598–610. doi: 10.1002/mrm.26402.

18. Huang J, Chen C, Axel L. Fast multi-contrast MRI reconstruction. Magn. Reson. Imaging [Internet] 2014;32:1344–1352. doi: 10.1016/j.mri.2014.08.025.

19. Ehrhardt MJ, Betcke MM. Multi-Contrast MRI Reconstruction with Structure-Guided Total Variation. SIAM J. Imaging Sci. [Internet] 2016;9:1084–1106. doi: 10.1137/15M1047325.

20. Majumdar A, Ward RK. Joint reconstruction of multiecho MR images using correlated sparsity. Magn. Reson. Imaging [Internet] 2011;29:899–906. doi: 10.1016/j.mri.2011.03.008.

21. Knoll F, Holler M, Koesters T, Otazo R, Bredies K, Sodickson DK. Joint MR-PET Reconstruction Using a Multi-Channel Image Regularizer. IEEE Trans. Med. Imaging 2017;36:1–16. doi: 10.1109/TMI.2016.2564989.

22. Peng X, Ying L, Liu Y, Yuan J, Liu X, Liang D. Accelerated exponential parameterization of T2 relaxation with model-driven low rank and sparsity priors (MORASA). Magn. Reson. Med. 2016;76:1865–1878. doi: 10.1002/mrm.26083.

23. Tamir JI, Uecker M, Chen W, Lai P, Alley MT, Vasanawala SS, Lustig M. T2 shuffling: Sharp, multicontrast, volumetric fast spin-echo imaging. Magn. Reson. Med. 2017;77:180–195. doi: 10.1002/mrm.26102.

24. Zhao B, Lu W, Hitchens TK, Lam F, Ho C, Liang ZP. Accelerated MR parameter mapping with low-rank and sparsity constraints. Magn. Reson. Med. 2015;74:489–498. doi: 10.1002/mrm.25421.

25. Trzasko J, Manduca A. Local versus Global Low-Rank Promotion in Dynamic MRI Series Reconstruction. Proc Intl Soc Mag Reson Med 2011;24:4371.

26. Zhang T, Pauly JM, Levesque IR. Accelerating parameter mapping with a locally low rank constraint. Magn. Reson. Med. 2015;73:655–661. doi: 10.1002/mrm.25161.

27. Zhang T, Cheng JY, Potnick AG, Barth RA, Alley MT, Uecker M, Lustig M,

598 Pauly JM, Vasanawala SS. Fast pediatric 3D free-breathing abdominal dynamic
599 contrast enhanced MRI with high spatiotemporal resolution. J. Magn. Reson.
600 Imaging 2015. doi: 10.1002/jmri.24551.
601 28. Christodoulou AG, Shaw JL, Nguyen C, Yang Q, Xie Y, Wang N, Li D. Magnetic
602 resonance multitasking for motion-resolved quantitative cardiovascular imaging.
603 Nat. Biomed. Eng. [Internet] 2018;2:215–226. doi: 10.1038/s41551-018-0217-y.
604 29. Shaw JL, Yang Q, Zhou Z, Deng Z, Nguyen C, Li D, Christodoulou AG. Free-
605 breathing, non-ECG, continuous myocardial T_1 mapping with cardiovascular
606 magnetic resonance Multitasking. Magn. Reson. Med. [Internet] 2018:1–14. doi:
607 10.1002/mrm.27574.
608 30. Akçakaya M, Basha TA, Chan RH, Manning WJ, Nezafat R. Accelerated
609 isotropic sub-millimeter whole-heart coronary MRI: Compressed sensing versus
610 parallel imaging. Magn. Reson. Med. 2014;71:815–822. doi: 10.1002/mrm.24683.
611 31. Bustin A, Voilliot D, Menini A, Felblinger J, de Chillou C, Burschka D,
612 Bonnemains L, Odille F. Isotropic Reconstruction of MR Images using 3D Patch-
613 Based Self-Similarity Learning. IEEE Trans. Med. Imaging 2018;37:1932–1942.
614 doi: 10.1109/TMI.2018.2807451.
615 32. Akçakaya M, Basha TA, Goddu B, Goepfert LA, Kissinger K V., Tarokh V,
616 Manning WJ, Nezafat R. Low-dimensional-structure self-learning and thresholding:
617 Regularization beyond compressed sensing for MRI Reconstruction. Magn. Reson.
618 Med. 2011;66:756–767. doi: 10.1002/mrm.22841.
619 33. Bustin A, Ginami G, Cruz G, Correia T, Ismail TF, Rashid I, Neji R, Botnar RM,
620 Prieto C. Five-minute whole-heart coronary MRA with sub-millimeter isotropic
621 resolution, 100% respiratory scan efficiency, and 3D-PROST reconstruction. Magn.
622 Reson. Med. [Internet] 2018;00:1–14. doi: 10.1002/mrm.27354.
623 34. Boyd S, Parikh N, Chu E, Peleato B, Eckstein J. Distributed Optimization and
624 Statistical Learning via the Alternating Direction Method of Multipliers. Found.

625 Trends Mach. Learn. [Internet] 2011;3:1–122. doi: 10.1561/2200000016.
626 35. Hestenes MR, Stiefel E. Methods of conjugate gradients for solving linear
627 systems. J. Res. Natl. Bur. Stand. (1934). [Internet] 1952;49:409. doi:
628 10.6028/jres.049.044.
629 36. De Lathauwer L, De Moor B, Vandewalle J. A multilinear singular value
630 decomposition. SIAM J. Matrix Anal. Appl. 2000. doi:
631 10.1137/S0895479896305696.
632 37. Tucker LR. Some mathematical notes on three-mode factor analysis.
633 Psychometrika 1966. doi: 10.1007/BF02289464.
634 38. Zhao B, Setsompop K, Adalsteinsson E, Gagoski B, Ye H, Ma D, Jiang Y, Ellen
635 Grant P, Griswold MA, Wald LL. Improved magnetic resonance fingerprinting
636 reconstruction with low-rank and subspace modeling. Magn. Reson. Med.
637 2018;79:933–942. doi: 10.1002/mrm.26701.
638 39. Assländer J, Cloos MA, Knoll F, Sodickson DK, Hennig J, Lattanzi R. Low rank
639 alternating direction method of multipliers reconstruction for MR fingerprinting.
640 Magn. Reson. Med. 2018;79:83–96. doi: 10.1002/mrm.26639.
641 40. Tang S, Fernandez-Granda C, Lannuzel S, Bernstein B, Lattanzi R, Cloos M,
642 Knoll F, Assländer J. Multicompartment Magnetic Resonance Fingerprinting. arXiv
643 Prepr. arXiv1802.10492 [Internet] 2018.
644 41. Doneva M, Amthor T, Koken P, Sommer K, Börnert P. Matrix completion-based
645 reconstruction for undersampled magnetic resonance fingerprinting data. Magn.
646 Reson. Imaging [Internet] 2017;41:41–52. doi: 10.1016/j.mri.2017.02.007.
647 42. Cline CC, Chen X, Mailhe B, Wang Q, Pfeuffer J, Nittka M, Griswold MA,
648 Speier P, Nadar MS. AIR-MRF: Accelerated iterative reconstruction for magnetic
649 resonance fingerprinting. Magn. Reson. Imaging [Internet] 2017;41:29–40. doi:
650 10.1016/j.mri.2017.07.007.
651 43. Captur G, Gatehouse P, Keenan KE, et al. A medical device-grade T1 and ECV

652 phantom for global T1 mapping quality assurance - the T1 Mapping and ECV
653 Standardization in cardiovascular magnetic resonance (T1MES) program. J.
654 Cardiovasc. Magn. Reson. [Internet] 2016;18:1–20. doi: 10.1186/s12968-016-0280-
655 z.
656 44. Assländer J, Lattanzi R, Sodickson DK, Cloos MA. Relaxation in Spherical
657 Coordinates: Analysis and Optimization of pseudo-SSFP based MR-Fingerprinting.
658 arXiv Prepr. arXiv1703.00481. [Internet] 2017:1–22. doi:
659 10.1017/CBO9781107415324.004.
660 45. Uecker M, Lai P, Murphy MJ, Virtue P, Elad M, Pauly JM, Vasanawala SS,
661 Lustig M. ESPIRiT-an eigenvalue approach to autocalibrating parallel MRI: Where
662 SENSE meets GRAPPA. Magn. Reson. Med. [Internet] 2013;194:990–1001. doi:
663 10.1002/mrm.24751.
664 46. Greengard L, Lee J-Y. Accelerating the Nonuniform Fast Fourier Transform.
665 SIAM Rev. [Internet] 2004;46:443–454. doi: 10.1137/S003614450343200X.
666 47. Weigel M. Extended phase graphs: Dephasing, RF pulses, and echoes - Pure and
667 simple. J. Magn. Reson. Imaging 2015;41:266–295. doi: 10.1002/jmri.24619.
668 48. Ma D, Coppo S, Chen Y, McGivney DF, Jiang Y, Pahwa S, Gulani V, Griswold
669 MA. Slice profile and B1 corrections in 2D magnetic resonance fingerprinting.
670 Magn. Reson. Med. 2017;78:1781–1789. doi: 10.1002/mrm.26580.
671 49. Prieto C, Doneva M, Usman M, Henningsson M, Greil G, Schaeffter T, Botnar
672 RM. Highly efficient respiratory motion compensated free-breathing coronary mra
673 using golden-step Cartesian acquisition. J. Magn. Reson. Imaging [Internet]
674 2015;41:738–746. doi: 10.1002/jmri.24602.
675 50. Otazo R, Candès E, Sodickson DK. Low-rank plus sparse matrix decomposition
676 for accelerated dynamic MRI with separation of background and dynamic
677 components. Magn. Reson. Med. 2015;73:1125–1136. doi: 10.1002/mrm.25240.
678 51. Tamir JI, Ong F, Cheng JY, Uecker M, Lustig M. Generalized Magnetic

679 Resonance Image Reconstruction using The Berkeley Advanced Reconstruction
680 Toolbox. Proc. ISMRM Work. Data Sampl. Ina. Reconstr. Sedona, AZ [Internet]
681 2016:33. doi: 10.5281/zenodo.31907.
682 52. Buonincontri G, Sawiak SJ. MR fingerprinting with simultaneous B1 estimation.
683 Magn. Reson. Med. 2016;76:1127–1135. doi: 10.1002/mrm.26009.
684 53. Hilbert T, Kober T, Zhao T, Block T, Yu Z, Thiran J-P, Krueger G, Sodickson
685 D, Cloos M. Mitigating the Effect of Magnetization Transfer in Magnetic Resonance
686 Fingerprinting. In: Proceedings of the 25th Annual Meeting of ISMRM Hawaii USA.
687 ; 2018. p. 74.
688 54. Kobayashi Y, Tereda Y. Diffusion-weighting caused by spoiler gradients in the
689 fast imaging with steady-state precession sequence may lead to inacurate T2
690 measurements in MR fingerprinting. Magn Reson Med Sci 2018. doi:
691 https://doi.org/10.2463/mrms.tn.2018-0027.
692 55. Murphy M, Alley M, Demmel J, Keutzer K, Vasanawala S, Lustig M. Fast l_1-
693 SPIRiT compressed sensing parallel imaging MRI: scalable parallel implementation
694 and clinically feasible runtime. IEEE Trans. Med. Imaging 2012. doi:
695 10.1109/TMI.2012.2188039.
696 56. Zhang T, Pauly JM, Vasanawala SS, Lustig M. Coil compression for accelerated
697 imaging with Cartesian sampling. Magn. Reson. Med. [Internet] 2013;69:571–82.
698 doi: 10.1002/mrm.24267.
699 57. Otazo R, Kim D, Axel L, Sodickson DK. Combination of compressed sensing
700 and parallel imaging for highly accelerated first-pass cardiac perfusion MRI. Magn.
701 Reson. Med. 2010;64:767–776. doi: 10.1002/mrm.22463.
702 58. Cheng JY, Zhang T, Alley MT, Uecker M, Lustig M, Pauly JM, Vasanawala SS.
703 Comprehensive Multi-Dimensional MRI for the Simultaneous Assessment of
704 Cardiopulmonary Anatomy and Physiology. Sci. Rep. 2017;7:5330. doi:
705 10.1038/s41598-017-04676-8.

59. Detre JA, Leigh JS, Williams DS, Koretsky AP. Perfusion imaging. Magn. Reson. Med. 1992. doi: 10.1002/mrm.1910230106.

Figure Captions

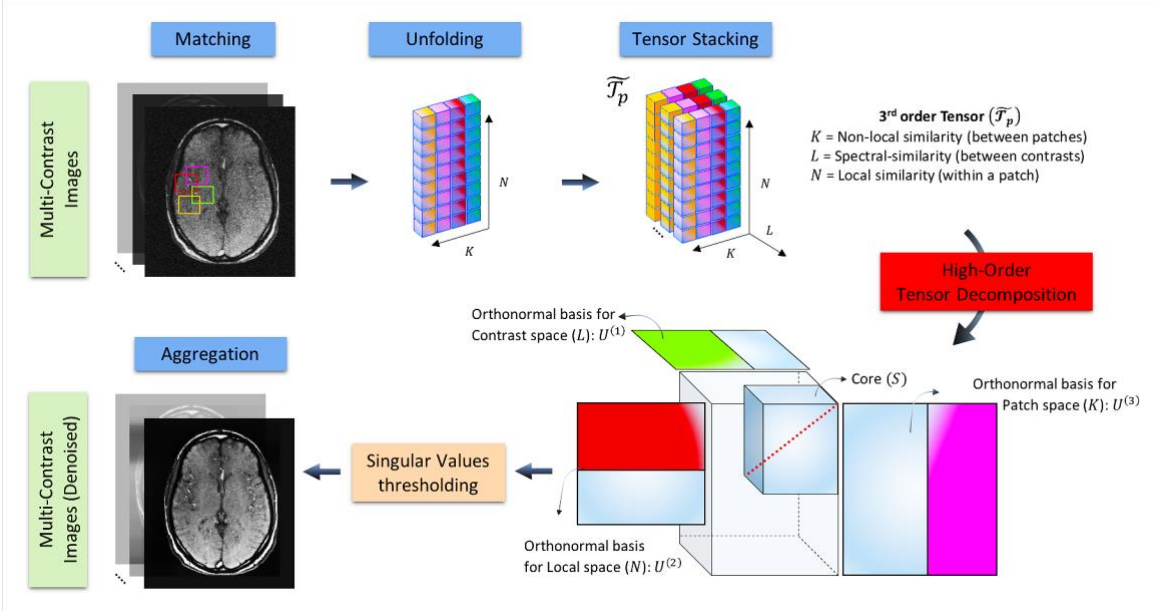

Figure 1: Flowchart of the optimization 2 of the proposed High-Dimensionality Patch-based RecOnSTruction (HD-PROST). Denoising of multi-contrast images is performed using 2D (respectively 3D) block matching, which groups similar 2D (respectively 3D) patches in the multi-contrast images. Similar patches are then unfolded together in a simple 2D matrix. A third-order tensor $\mathcal{T}$ is formed by stacking the unfolded patches in the contrast dimension. The high-order tensor of size $N \times K \times L$ admits a low multilinear rank approximation and can be compressed, through tensor decomposition, by truncating the multilinear singular vectors that correspond to small multilinear singular values. The outputs of this step are the denoised multi-contrast images which are then used in the joint MR reconstruction process (optimization 1) as prior knowledge. An overview of the algorithm is provided in Supporting Information Table S1.

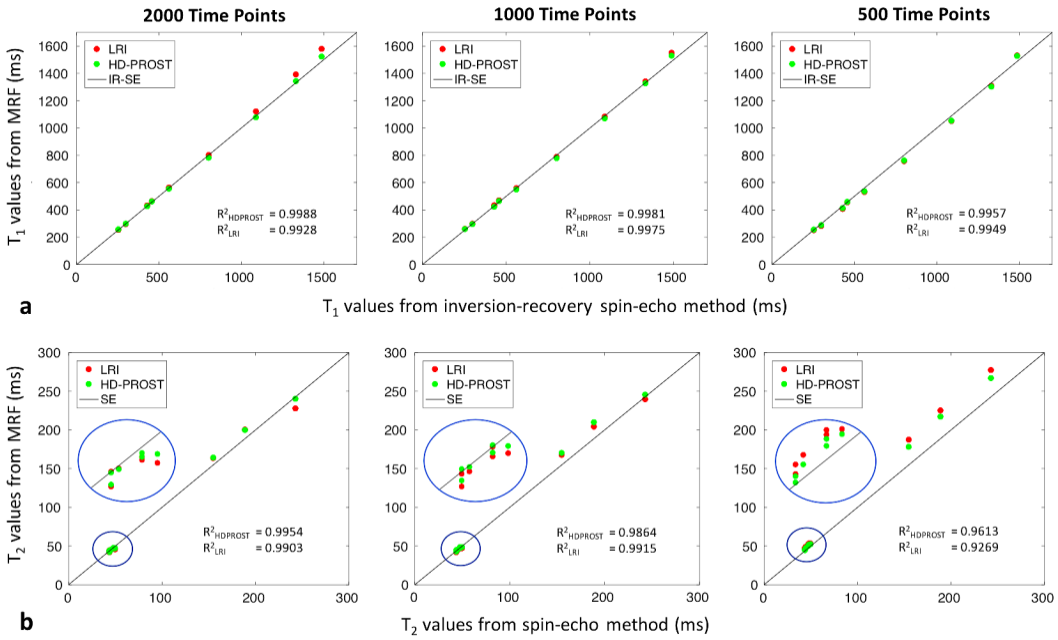

722

723 **Figure 2:** Phantom results for the 2D accelerated MRF using low-rank inversion (LRI) and
724 the proposed HD-PROST reconstructions. Plots are comparing the mean T_1 (a) and T_2 (b)
725 values derived from 2000, 1000 and 500 time-points, with conventional inversion-recovery
726 spin-echo (IRSE) and spin-echo (SE) acquisitions (identity lines). T_1 and T_2 accuracies are
727 preserved with the two strategies, with a slight bias observed for long T2s at high
728 accelerations for both methods. The mean values were obtained from ROIs drawn around
729 each phantom vial. Abbreviations – LRI: low-rank inversion, HD-PROST: high-
730 dimensionality undersampled patch-based reconstruction.

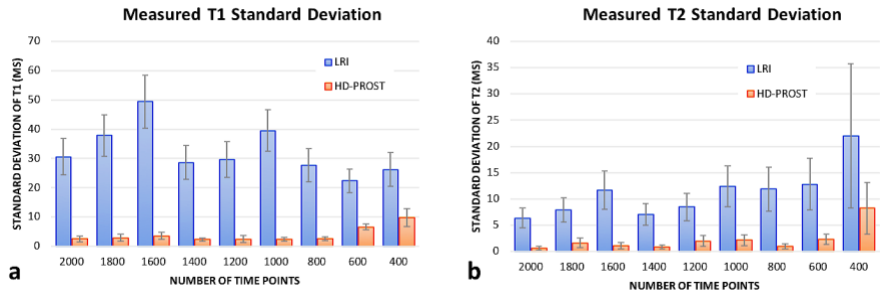

731

732 **Figure 3:** Standard deviations of T_1 (a) and T_2 (b) relaxation times for the phantom study
733 are shown for LRI and HD-PROST reconstructions for [400:200:2000] acquired time-point
734 images. The precision, as indicated by the standard deviation, was considerably higher with

the proposed HD-PROST reconstruction, even for shorter acquisitions, while LRI resulted in systematic higher standard deviations. The standard deviations were obtained from ROIs drawn around each phantom vial. Abbreviations – LRI: low-rank inversion, HD-PROST: high-dimensionality undersampled patch-based reconstruction.

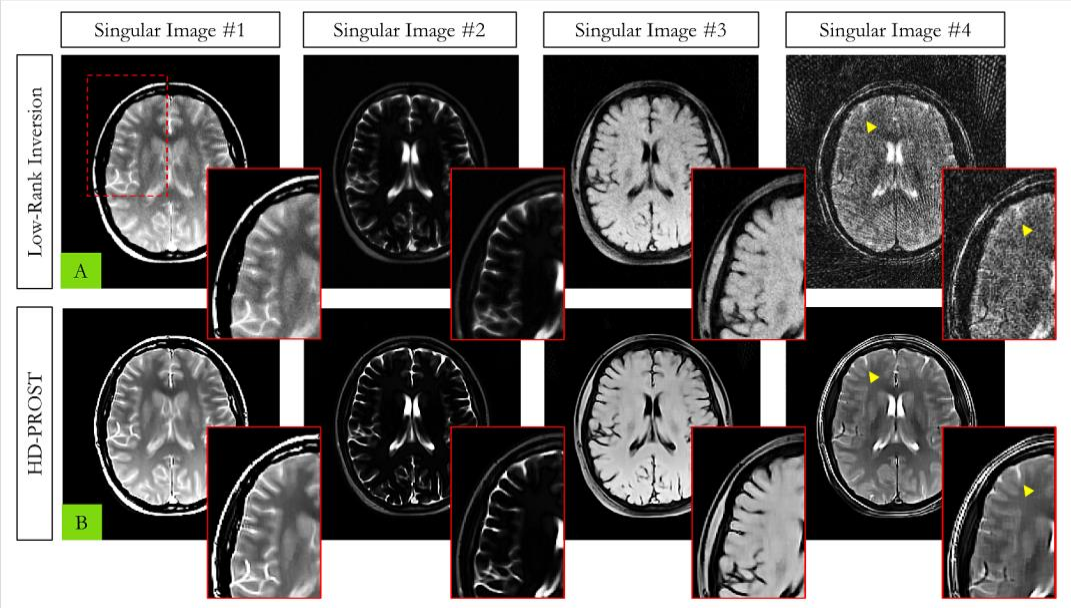

Figure 4: Reconstructed first four MRF singular images with low-rank inversion (LRI) (a) and the proposed HD-PROST (b) in in vivo brain experiments in a representative subject acquired with 1000 time-points. A clear improvement in image quality and image sharpness can be observed on the HD-PROST reconstruction with considerable reduction of noise and streaking artifacts, particularly for the last singular images.

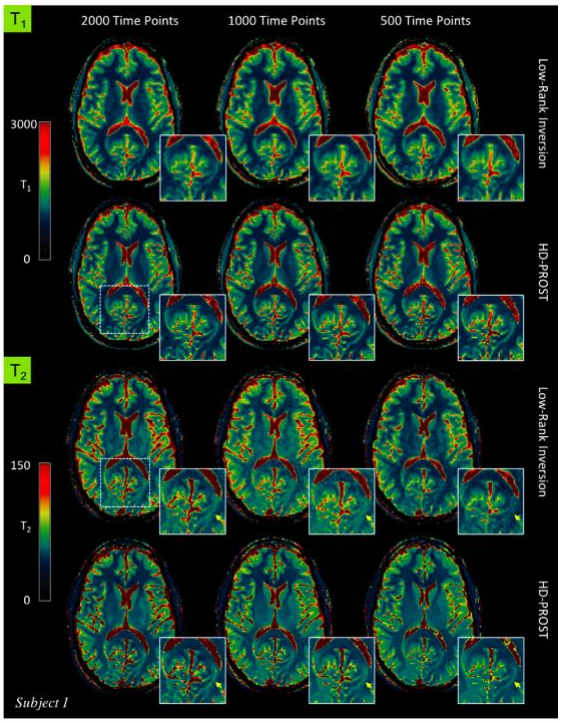

Figure 5: In vivo MRF-derived quantitative T_1 (top) and T_2 (bottom) maps for subject 1 reconstructed with low-rank inversion (LRI) MRF and the proposed HD-PROST reconstruction with 2000, 1000 and 500 time-points.

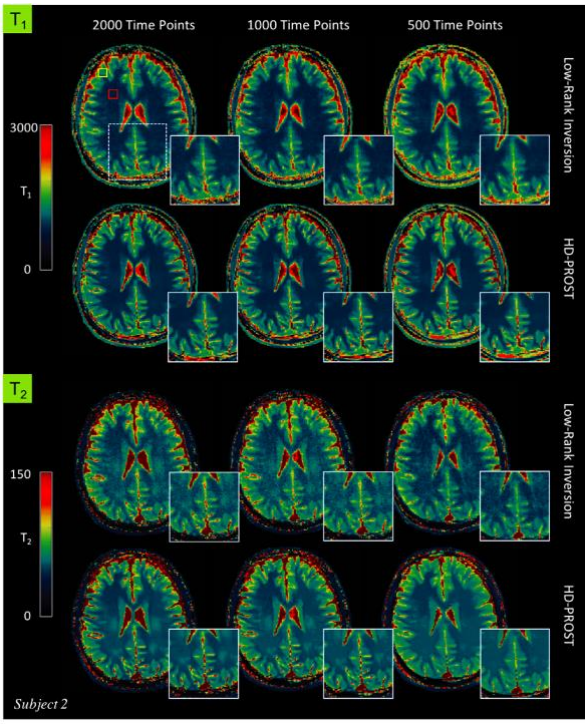

Figure 6: T_1 (top) and T_2 (bottom) maps for subject 2 reconstructed with low-rank inversion (LRI) MRF and the proposed HD-PROST reconstruction with 2000, 1000 and 500 time-points. The yellow and red rectangles on the top-left map indicate the regions of interest used to determine the T_1 and T_2 relaxation times (see Table 1).

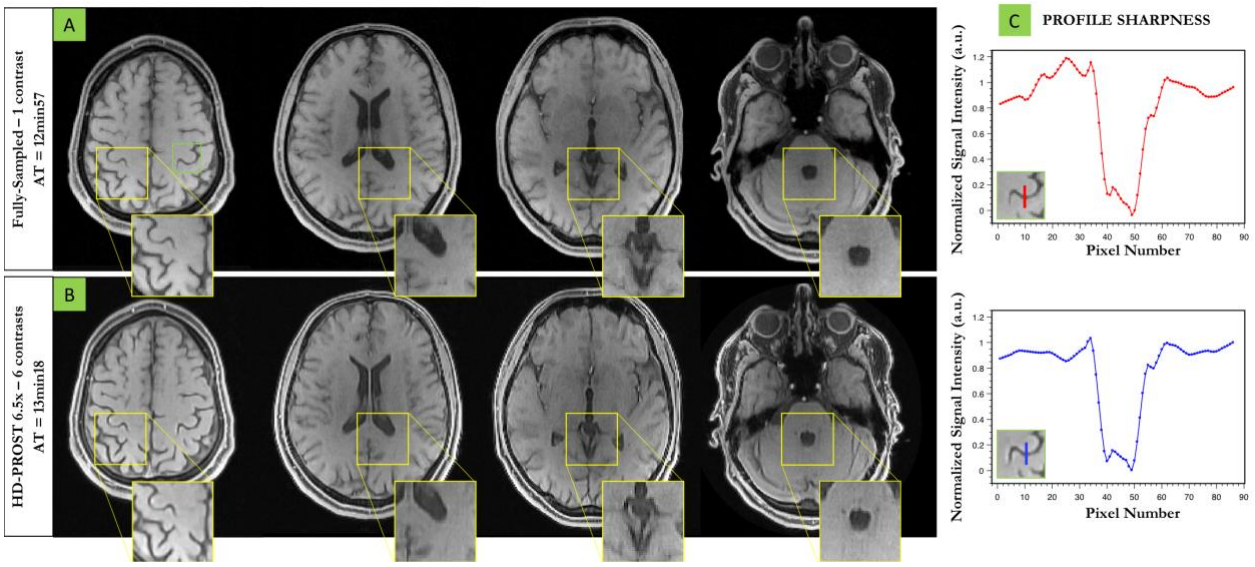

Figure 7: Three-dimensional reconstruction of a MT-weighted 6.5-fold undersampled brain data in a healthy subject (subject 1). HD-PROST reconstruction (B) is compared to the fully-sampled acquisition (A) for the reference image only ($\alpha_{MT} = 0°$). Line profiles going through a structure with sharp edges are shown in (C). HD-PROST is able to recover high fidelity 3D images and retrieve sharp edges in agreement with the fully-sampled acquisition. Six different undersampled MT-weighted images were acquired in 13min 18s, whereas the fully-sampled acquisition of a single contrast took 12min 57s.

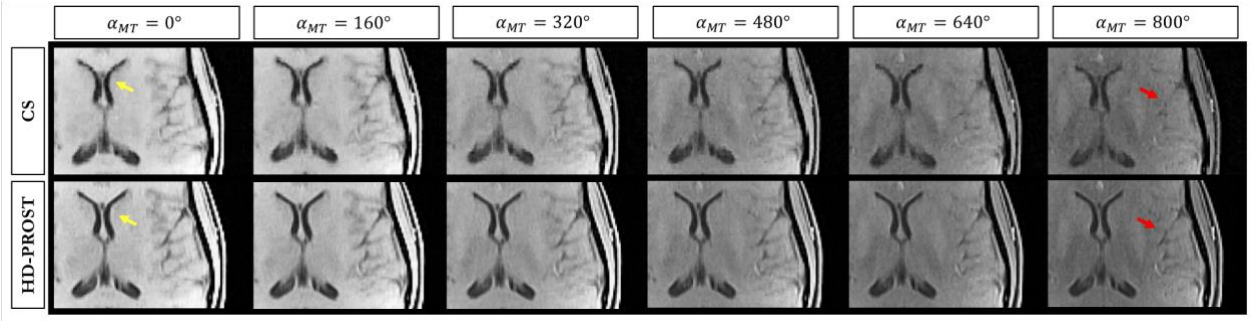

Figure 8: 6.5-fold accelerated 3D MT-weighted images for 6 different contrasts from one representative subject (subject 1) reconstructed with compressed-sensing (CS), and the proposed HD-PROST reconstruction. Fine anatomical structures can be efficiently retrieved with HD-PROST as shown by the arrows. See Supporting Information Figure S5 for the visualization of the whole axial images and Supporting Information Figure S6 for comparisons with zero-filling and locally low-rank reconstructions.

Table Captions

Table 1: T_1 and T_2 relaxation times at 1.5T for low-rank inversion (LRI) and the proposed HD-PROST in regions of interest covering white and grey matters in the five healthy subjects (regions of interest are drawn in the maps in Figure 6). Values are shown for different MRF measurement lengths and compared with the corresponding literature values.

		T_1 (ms)			T_2 (ms)		
	#Time points	**LRI**	**HD-PROST**	**Literature**	**LRI**	**HD-PROST**	**Literature**
White Matter	2000	737 ± 61	743 ± 37	608 – 756	45 ± 5	45 ± 4	54 – 81
	1000	718 ± 63	732 ± 36		47 ± 6	46 ± 4	
	500	741 ± 64	746 ± 44		42 ± 4	45 ± 3	
Grey Matter	2000	999 ± 117	992 ± 106	998 – 1034	55 ± 6	54 ± 4	78 – 98
	1000	988 ± 125	982 ± 108		57 ± 6	56 ± 4	
	500	1059 ± 151	1024 ± 128		52 ± 7	55 ± 4	

Abbreviations − LRI: low-rank inversion, HD-PROST: high-dimensionality undersampled patch-based reconstruction. Values are expressed as mean ± SD

Supporting Information Figure Captions

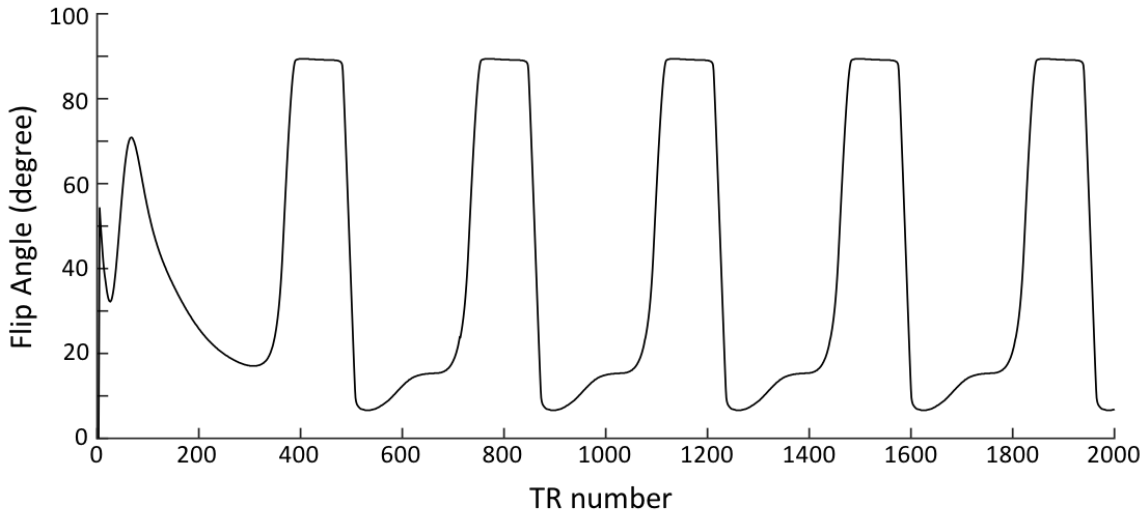

Supporting Information Figure S1: Variable flip angle pattern used in the accelerated 2D MRF study. This pattern was described in Assländer et al. (44).

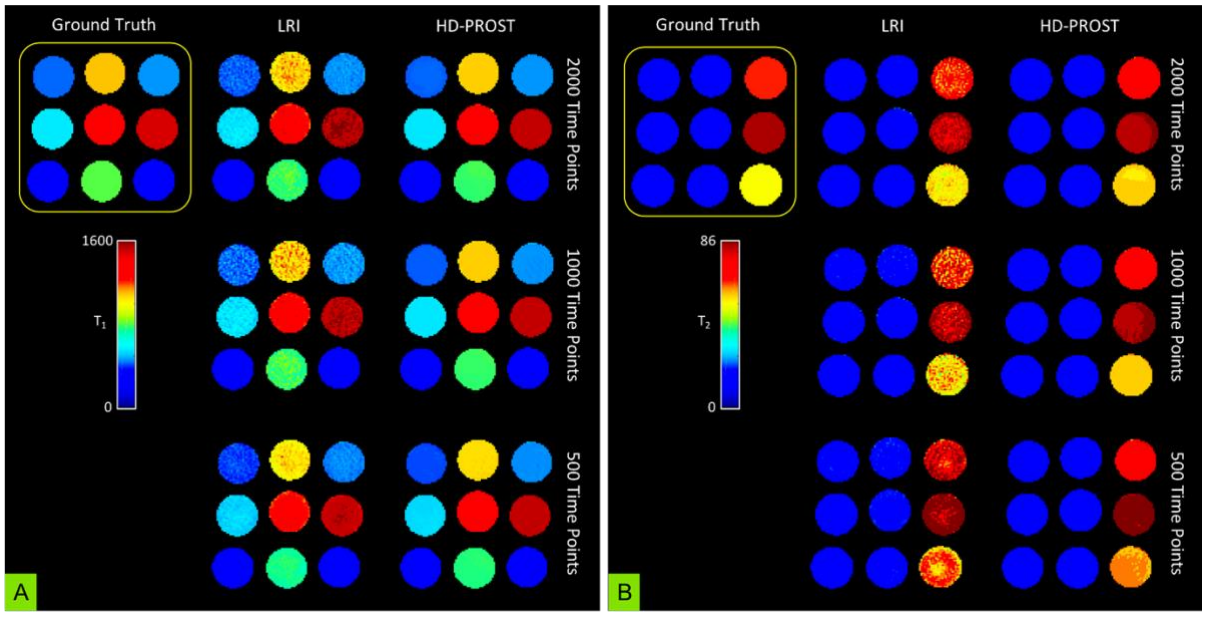

Supporting Information Figure S2: T_1 map (A) and T_2 map (B) of the 2D MRF phantom acquisition. The quantitative values for all phantom tubes are reported in Figure 2. Abbreviations – LRI: low-rank inversion, HD-PROST: high-dimensionality undersampled patch-based reconstruction.

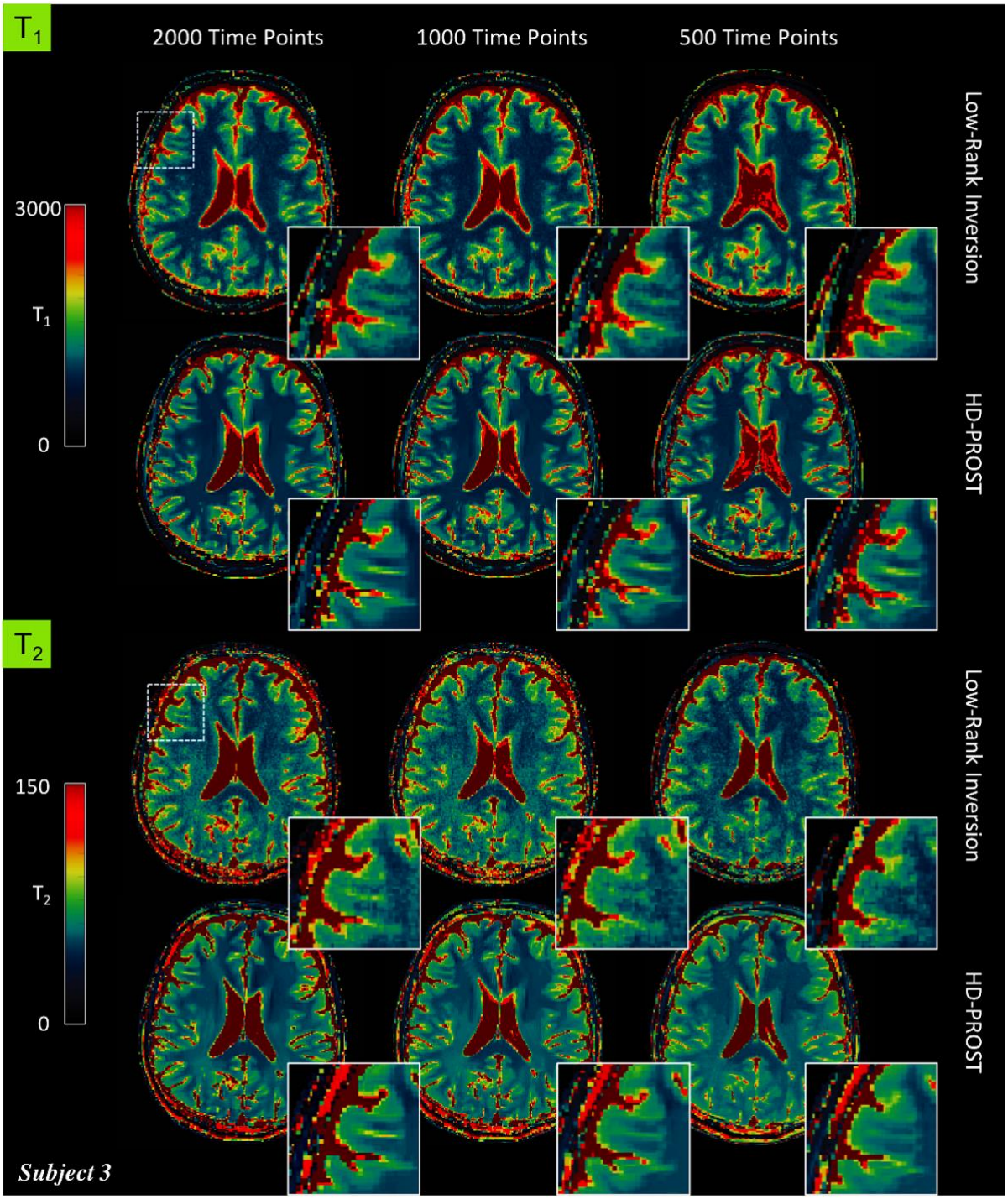

Supporting Information Figure S3: T_1 (top) and T_2 (bottom) maps for subject 3 reconstructed with low-rank inversion MRF and the proposed HD-PROST reconstruction with 2000, 1000 and 500 time-points.

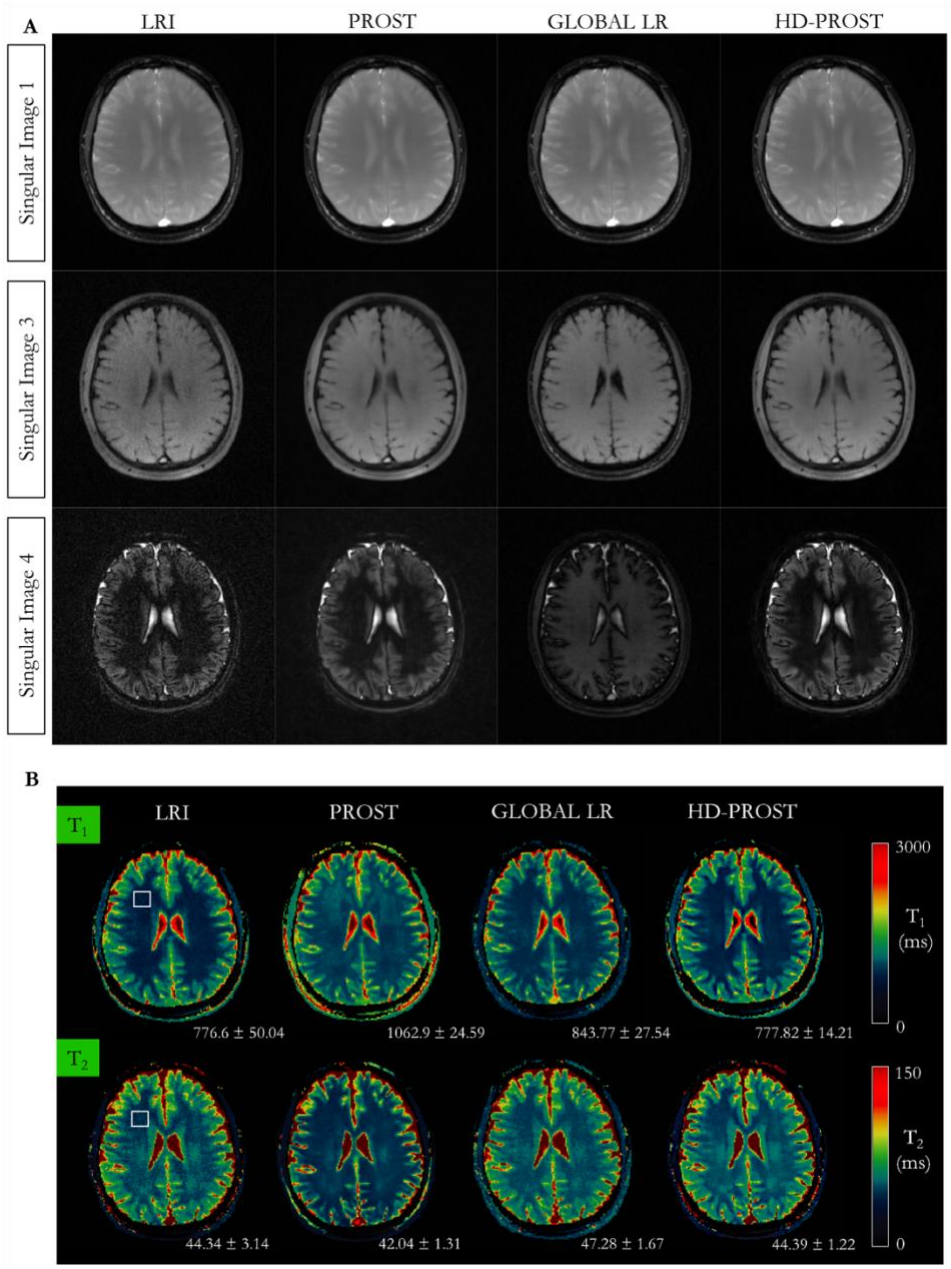

799

800 **Supporting Information Figure S4:** 2D MRF singular images (A) and corresponding T_1
801 (top) and T_2 (bottom) maps (B) for subject 2 reconstructed with low-rank inversion (LRI),
802 PROST (i.e. reconstructing each MRF singular image independently), global low-rank
803 tensor decomposition (global LR) and the proposed HD-PROST reconstruction. The white
804 rectangle on the top-left map indicates the region of interest used to determine the T_1 an T_2
805 relaxation times. By exploiting local, non-local and contrast redundancies, the proposed
806 HD-PROST technique obtains better performance than the other techniques and
807 reconstructs high-quality T_1 and T_2 maps with great noise-like artefacts reduction, contrast

preservation, as well as sharpness enhancement, with T_1 and T_2 accuracies similar to the unregularized LRI reconstruction.

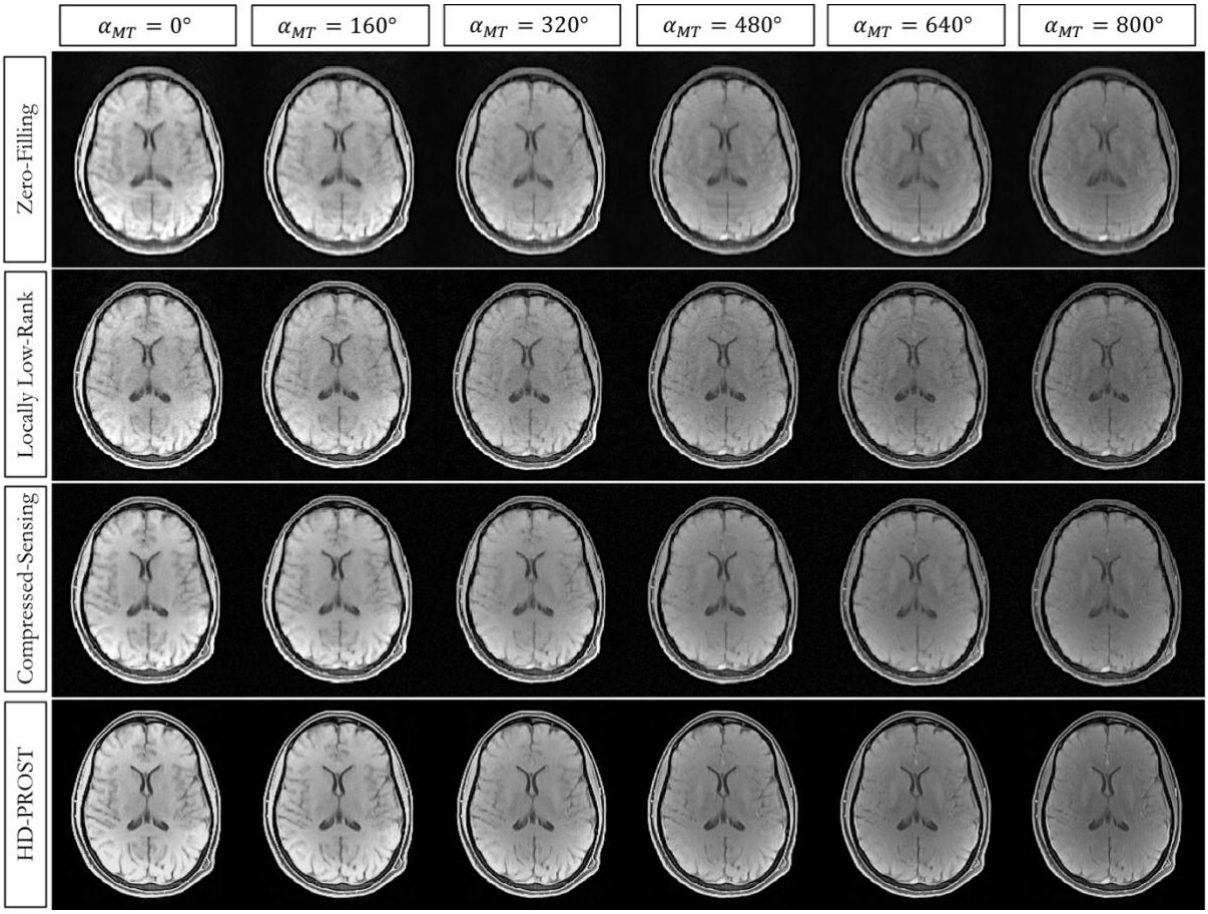

Supporting Information Figure S5: 6.5-fold accelerated 3D MT-weighted images for 6 different contrasts from subject 1 reconstructed with zero-filling, locally low-rank, compressed-sensing, and the proposed HD-PROST.

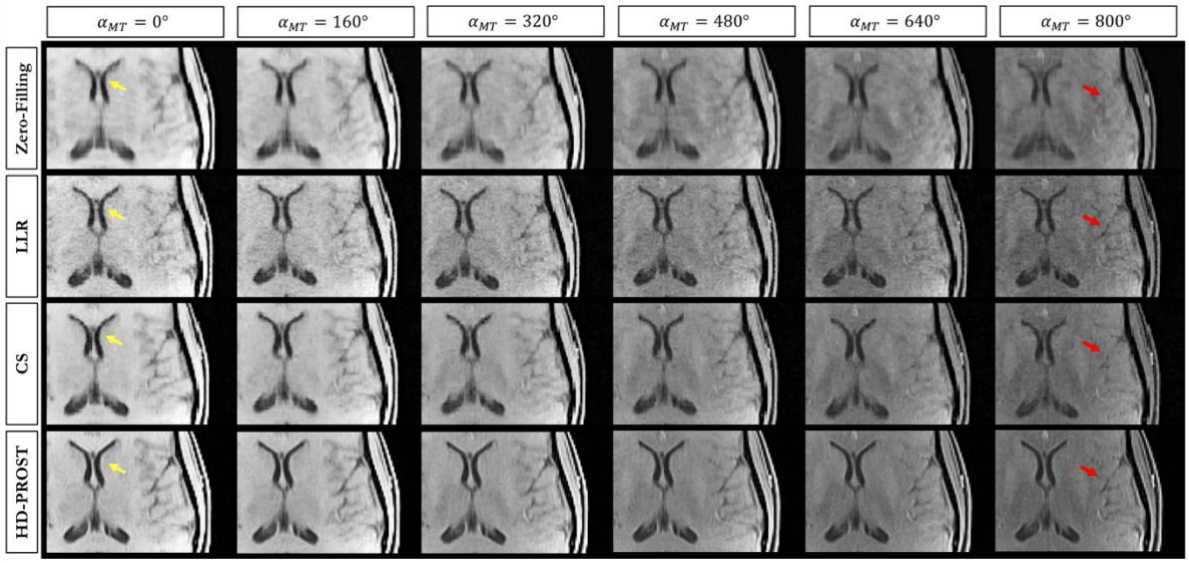

Supporting Information Figure S6: 6.5-fold accelerated 3D MT-weighted images for 6 different contrasts from one representative subject (subject 1) reconstructed with zero-filling, locally low-rank (LLR), compressed-sensing (CS), and the proposed HD-PROST. Fine anatomical structures can be efficiently retrieved with HD-PROST as shown by the arrows. See Supporting Information Figure S5 for the visualization of the whole axial images. Note that slight residual motion can be observed on the sharp HD-PROST reconstruction, which is lost in blurring on the compressed sensing reconstruction (due to regularization) and in the noise of LLR reconstruction.

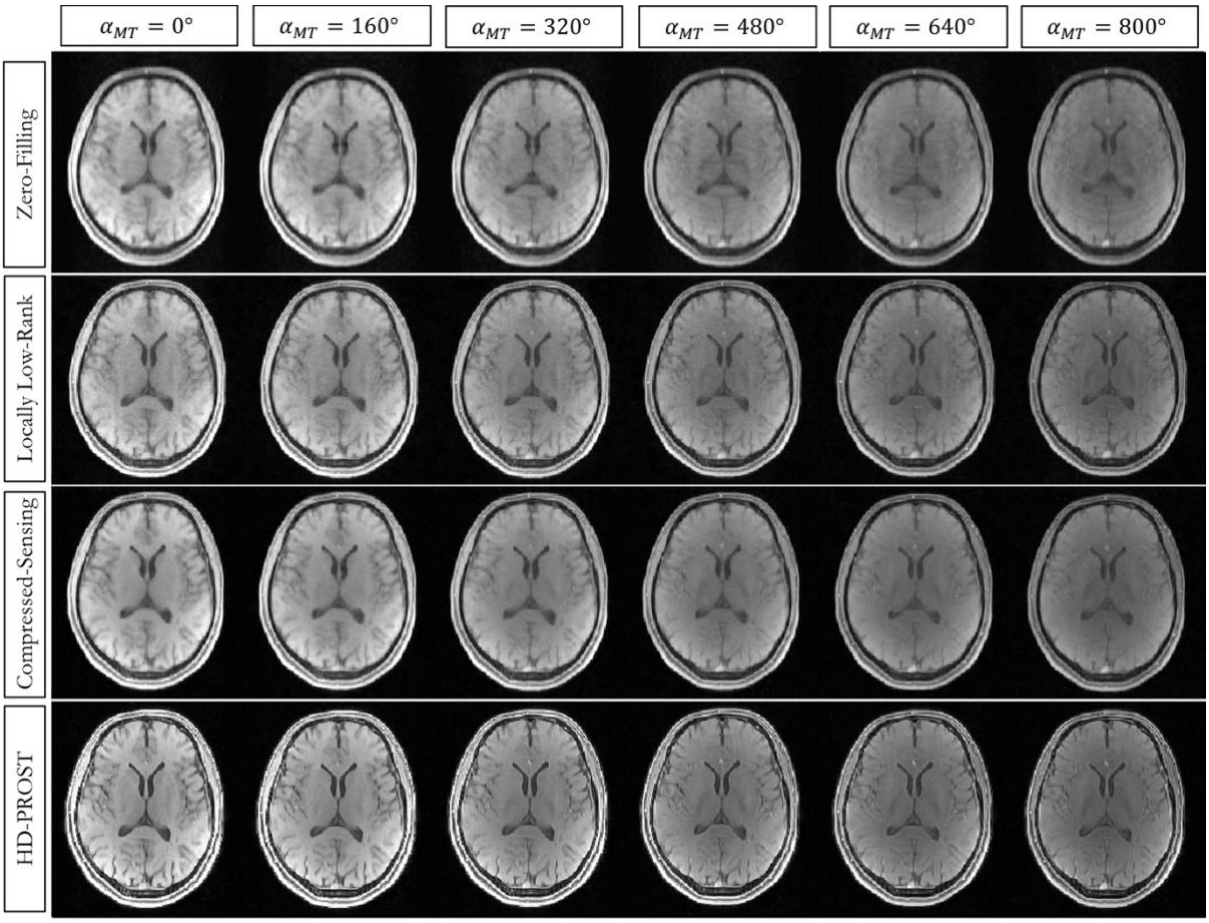

Supporting Information Figure S7: 6.5-fold accelerated 3D MT-weighted images for 6 different contrasts from subject 2 reconstructed with zero-filling, locally low-rank, compressed-sensing , and the proposed HD-PROST.

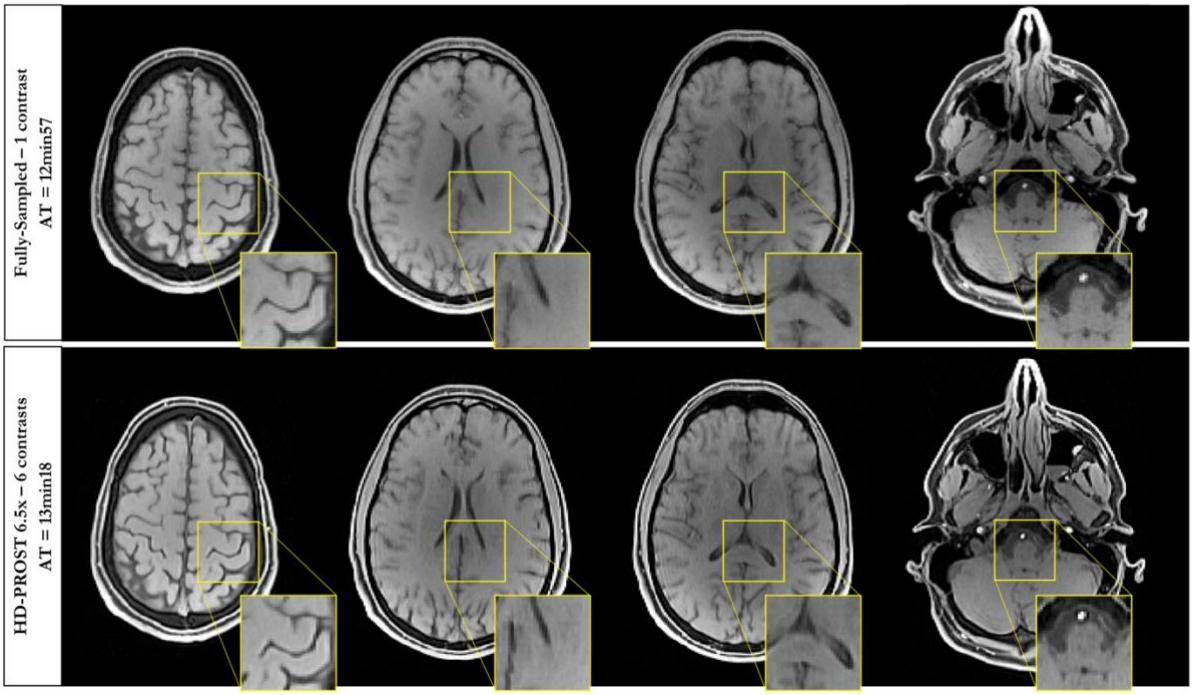

Supporting Information Figure S8: Three-dimensional reconstruction of a MT-weighted 6.5-fold undersampled brain data in a healthy subject (subject 3). HD-PROST reconstruction is compared to the fully-sampled acquisition for the reference image only ($\alpha_{MT} = 0°$). Six different undersampled MT-weighted images were acquired in 13min 18s, whereas the fully-sampled acquisition of a single contrast took 12min 57s.

Supporting Information Table Captions

ALGORITHM I

HIGH-ORDER TENSOR DECOMPOSITION ALGORITHM FOR HD-PROST RECONSTRUCTION

INPUT: *data tensor* $\mathcal{T}$ *with dimensions* (N, K, L) *and regularization parameter* λ

ALGORITHM:

(1) Unfold the tensor $\mathcal{T}$ *along its single modes:*

$\mathcal{T}_1$*: which reshapes* $\mathcal{T}$ *into a* $L \times (N \,.\, K)$ *complex matrix*

$\mathcal{T}_2$*: which reshapes* $\mathcal{T}$ *into a* $N \times (L \,.\, K)$ *complex matrix*

$\mathcal{T}_3$*: which reshapes* $\mathcal{T}$ *into a* $K \times (L \,.\, N)$ *complex matrix*

(2) Compute the complex SVD of $\mathcal{T}_n$ *and get the orthogonal matrices* $U^{(1)}$, $U^{(2)}$, $U^{(3)}$ *from the* n^{th}*-mode signal subspace*

(3) Compute the complex core tensor $\boldsymbol{\mathcal{S}}$ *related by*

$$\mathcal{S} = \mathcal{T} \times_1 U_{(1)}^H \times_2 U_{(2)}^H \times_3 U_{(3)}^H$$

Which is equivalent to its unfolding forms:

$$\mathcal{S}_n = U_{(n)}^H \,.\, \mathcal{T}_n \cdot \left[U_{(i)} \otimes U_{(j)}\right] \quad with\ 1 \le n \le 3\ and\ i \ne j \ne n$$

In which $\otimes$ *denotes the Kronecker product*

(4) Compute the high-order singular values truncation (hard-thresholding):

$$\mathcal{S}(\mathcal{S} < \lambda) = 0$$

(5) Construct back the filtered tensor $\mathcal{T}_{(n)}^{den}$*:*

$$\mathcal{T}_{(n)}^{den} = U_{(n)} \,.\, \mathcal{S} \,.\, \left[U_{(i)} \otimes U_{(j)}\right]^H \ with\ 1 \le n \le 3\ and\ i \ne j \ne n$$

OUTPUT: *The denoised tensor* $\mathcal{T}^{den}$ *is obtained by folding*

Supporting Information Table S1: Algorithm I: high-order tensor decomposition algorithm for HD-PROST reconstruction.

ALGORITHM II
HIGH-DIMENSIONALITY UNDERSAMPLED PATCH-BASED RECONSTRUCTION (HD-PROST)

INPUT: *undersampled multi-channel multi-contrast images X*

parameters λ_p, μ*, ADMM iterations* $ADMM_{iter}$

Encoding operator E (coil sensitivities S*, sampling mask A)*

Compression operator U_r *(for MRF)*

INITIALIZATION:

Solve optimization 1 (Eq. 4): Joint MR reconstruction without prior ($\mu = 0$)

% ***Output****:* $X^{(0)}$

ALGORITHM:

$for\ i = 1, \dots, ADMM_{iter}$

Solve optimization 2 (Eq. 5): HOSVD-based denoising (see Algorithm I)

% ***Output****: denoised tensor* $\mathcal{T}^{(i)}$

Solve optimization 1 (Eq. 4): Joint MR reconstruction with prior

% ***Output****: reconstructed images* $\mathrm{X}^{(i)}$

Update Lagrangian multiplier:

$$b^{(i)} = b^{(i-1)} + X^{(i)} - \mathcal{T}^{(i)}$$

$end\ for$

OUTPUT: *The multi-contrast images X*

Supporting Information Table S2: Algorithm II: high-dimensionality undersampled patch-based reconstruction (HD-PROST).